Energy & Environmental Science

RSC Publishing

PAPER

# Highly active and durable nanostructured molybdenum carbide electrocatalysts for hydrogen production†

Cite this: *Energy Environ. Sci.*, 2013, **6**, 943

W.-F. Chen,[a] C.-H. Wang,[ab] K. Sasaki,*[a] N. Marinkovic,[c] W. Xu,[a] J. T. Muckerman,[a] Y. Zhu[b] and R. R. Adzic[a]

Received 24th October 2012
Accepted 19th December 2012

DOI: 10.1039/c2ee23891h

**www.rsc.org/ees**

In an attempt to tailor low-cost, precious-metal-free electrocatalysts for water electrolysis in acid, molybdenum carbide (β-$Mo_2C$) nanoparticles are prepared by *in situ* carburization of ammonium molybdate on carbon nanotubes and XC-72R carbon black without using any gaseous carbon source. The formation of $Mo_2C$ is investigated by thermogravimetry and *in situ* X-ray diffraction. X-ray absorption analysis reveals that $Mo_2C$ nanoparticles are inlaid or anchored into the carbon supports, and the electronic modification makes the surface exhibit a relatively moderate Mo–H bond strength. It is found that carbon nanotube-supported $Mo_2C$ showed superior electrocatalytic activity and stability in the hydrogen evolution reaction (HER) compared to the bulk $Mo_2C$. An overpotential of 63 mV for driving 1 mA $cm^{-2}$ of current density was measured for the nanotube-supported $Mo_2C$ catalysts; this exceeds the activity of analogous $Mo_2C$ catalysts. The enhanced electrochemical activity is facilitated by unique effects of the anchored structure coupled with the electronic modification.

**Broader context**

Splitting water into hydrogen by sustainable energy sources such as solar and wind power is a promising energy storage approach. Electrocatalytic systems for $H_2$ generation typically incorporate noble metals such as Pt in the catalysts because of their low overpotential and fast kinetics for driving the hydrogen evolution reaction (HER). However, replacement of presently available platinum catalysts by low-cost and earth-abundant materials is a requisite for this technology to become economically viable. The studies presented here report non-precious-metal electrocatalysts composed of molybdenum and carbon, and produced by a simple *in situ* carburization method. The catalysts are highly efficient for hydrogen production. We demonstrate the interplay of architectural and ligand effects in electrocatalytic activity and charge-transfer behavior of the anchored nanocatalysts.

## Introduction

The direct electrochemical splitting of water presents an attractive method to produce the renewable energy carrier hydrogen. The electrolysis efficiency is enhanced when Pt is used as the catalysts in acidic media. However, Pt remains to be an expensive metal and suffers from a shortage in global supply. Considerable attempts have been made recently to develop transition metal chalcogenides,[1–4] complexes[5] and metal carbides[6–11] for the purpose of replacing the Pt group metals. Among these catalysts molybdenum sulfide-based hydrogen evolution reaction (HER) catalysts have been investigated extensively.[12–14] Group VI transition metal carbides exhibit catalytic properties analogous to platinum group metals because of their unique d-band electronic structures.[15,16] Tungsten carbide has been intensively studied as an electrocatalyst for the HER by Chen's group[17,18] because of its potential to reduce the cost of PEM electrolyzers and its good stability in acid media. However, the required overpotential for catalyzing the HER on tungsten carbide is by far inferior to Pt-group metals. In regard to reducing the HER overpotential, corrosion studies on transition metal carbides by Weidman *et al.*[19] provided a hint as to how the overpotential might be reduced with molybdenum carbides.

In recent years, studies have shown that molybdenum carbides are active in a variety of catalytic reactions including desulfurization,[20,21] the water gas shift,[22] and hydrogenation reactions.[23,24] Very recently, Vrubel and Hu have investigated the use of commercial molybdenum carbide for electrochemical hydrogen production.[25] It is known that the catalytic properties of carbide materials strongly depend on their surface structure and composition, which are closely associated with their method of synthesis. Many approaches including chemical vapor deposition (CVD)[26,27] and pyrolysis of metal complexes[28–30]

[a]*Chemistry Department, Brookhaven National Laboratory, Upton, NY 11973, USA. E-mail: ksasaki@bnl.gov; Tel: +1 631 344 3446*

[b]*Condensed Matter Physics & Materials Science Department, Brookhaven National Laboratory, Upton, New York 11973, USA*

[c]*Department of Chemical Engineering, University of Delaware, Newark, Delaware 19716, USA*

† Electronic supplementary information (ESI) available: Decomposition mechanism, TGA profile, EXAFS spectra, electrical equivalent circuit models, Nyquist plots, and polarization curves. See DOI: 10.1039/c2ee23891h

have been developed for the preparation of metal carbides. Among these preparation methods, the representative one is CVD using carbonaceous gases, *e.g.*, $CH_4$, $C_2H_6$ and CO, and gaseous Mo-containing reagents, *e.g.*, $MoF_6$, $Mo(CO)_6$ and $MoCl_5$. However, some problems have been found with the gas-phase synthesis: the resultant carbide is usually contaminated by chars from the pyrolysis of the carbonaceous gases.[31] Chars block the pores, cover the active sites of the metal carbide, and are difficult to remove. Further, most of the gas-phase syntheses are cumbersome, require elaborate equipment, and involve the use of costly and toxic reagents. The gaseous Mo-precursors are hazardous substances and are harmful to living things and the environment.

In an effort to develop non-noble-metal materials for replacing Pt as an HER cathode, and to exploit the decrease in overpotential by carrying out the HER in acidic media, we have recently described a heterogeneous electrocatalytic hydrogen evolving system based on nickel molybdenum nitride nanosheets.[32] Despite the superior activity and good durability of the bimetallic nitride catalyst, its synthesis requires the use of hazardous ammonia gas. Here we report the synthesis of molybdenum carbide ($Mo_2C$) which is covalently anchored to carbon supports (carbon nanotubes and XC-72R carbon black) by a simple and environmentally friendly carburization process. High electrocatalytic performance for the HER with a low overpotential and high exchange current density is demonstrated, and is correlated with the structural and ligand effects of the anchored nanocatalysts.

## Results and discussion

### Formation of carbon-supported molybdenum carbide

The formation of molybdenum carbide from ammonium molybdate under an inert environment was carried out using a thermogravimetry/differential thermal analyzer (TG-DTA) and was probed by *in situ* time-resolved synchrotron X-ray diffraction (XRD). A typical thermal decomposition profile of XC-72R carbon-supported ammonium heptamolybdate (solid curves) is shown in Fig. 1a. The profile of unsupported ammonium heptamolybdate is also shown (dotted curves). A weight loss appeared below 300 °C on unsupported ammonium heptamolybdate, however, only slight loss was observed on a XC-72R carbon-supported sample. The first derivative of the TG profile of the carbon-supported sample (see Fig. S1 in the ESI†) reveals three apparent decreases in the sample's weight over the temperature range of 100–350 °C. These signals in weight loss correspond well to the endothermic peaks I, II and III as shown in Fig. 1a, which arise from the decomposition of ammonium molybdate; $MoO_3$ is thus formed.[33,34] For the unsupported sample, the sublimation of $MoO_3$ occurred at around 800 °C (steep weight loss accompanied by a prominent endothermic profile). In sharp contrast, no sublimation was observed on the carbon-supported sample. Instead, a major weight loss occurs at around 515 °C (a substantial weight change is observed in Fig. S1†), which corresponds to the reduction of $MoO_3$ to $MoO_2$. When holding the temperature at 800 °C, the gradual weight loss in the first hour is attributed to the formation of molybdenum carbide through the *in situ* solid-state reaction of carbon and $MoO_2$.

The powder X-ray diffraction (XRD) patterns of carbon-supported ammonium molybdate and the carburized product are compared in Fig. 1b. The carburized product was found to contain a pure orthorhombic β-$Mo_2C$ phase (JCPDS 77-0720). The calculated lattice constants $a = 6.012$, $b = 4.747$ and $c = 5.204$ are in good agreement with the reported values ($a = 6.002$, $b = 4.752$, and $c = 5.195$). The grain sizes calculated by the (211) peak are 11.2 nm for $Mo_2C$/XC and 14.2 nm for $Mo_2C$/CNT, respectively.

### Structural transformation during carburization

Structural transformation from ammonium molybdate to molybdenum carbide on XC-72R carbon was explicitly demonstrated by *in situ* time-resolved synchrotron XRD as shown in Fig. 2. The carbon-supported ammonium molybdate was loaded in a quartz tube reactor and was annealed from 25 to 800 °C with a pure He flow. The first pattern recorded at 25 °C exhibited a major monoclinic $(NH_4)_2Mo_3O_{10}$ crystal phase (JCPDS PDF

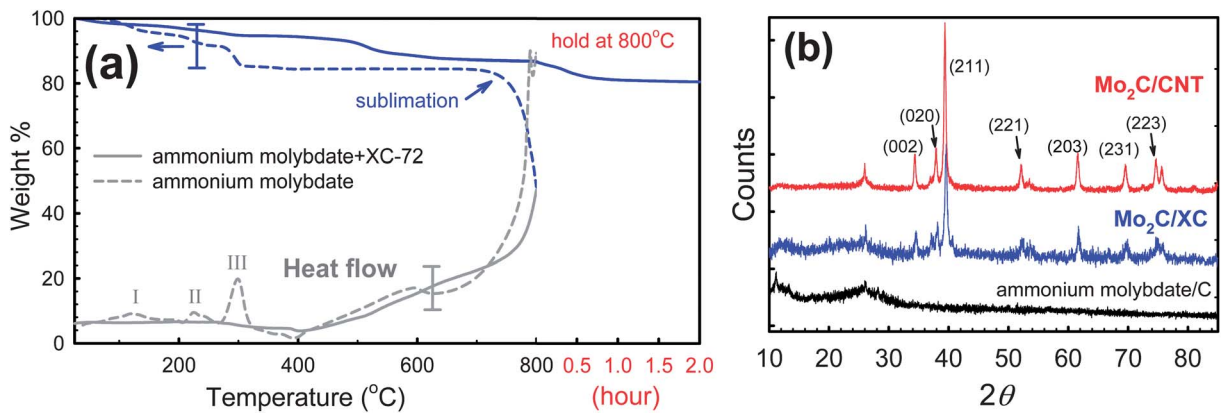


**Fig. 1** (a) TGA-DTA thermograms (blue curves) and the heat flow profiles (grey curves) of unsupported ammonium molybdate (dashed curves) and carbon-supported ammonium molybdate (solid curves) under Ar. (b) Powder XRD patterns of carbon-supported ammonium molybdate and the carburized products, $Mo_2C$/CNT and $Mo_2C$/XC.

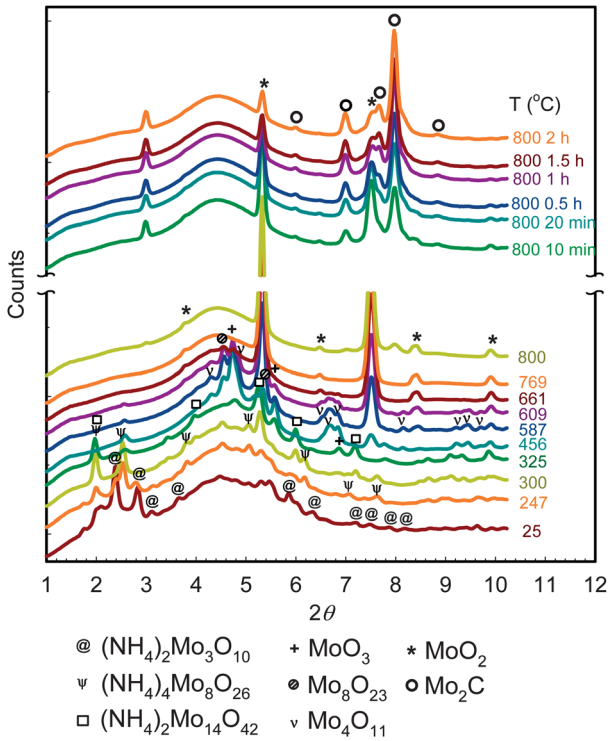


**Fig. 2** *In situ* time-resolved synchrotron XRD patters (wavelength: 0.3184 Å) of carbon-supported ammonium molybdate under He heated from room temperature to 800 °C and held at 800 °C for 2 h.

79-1905) which was produced while drying the carbon-supported $(NH_4)_2Mo_7O_{24}\cdot 4H_2O$. The decomposition of $(NH_4)_2Mo_3O_{10}$ at 247–609 °C resulted in several intermediates (see Scheme S1 in the ESI† for the decomposition steps) including triclinic $(NH_4)_4Mo_8O_{26}$ (JCPDS PDF 18-0117), hexagonal $(NH_4)_2Mo_{14}O_{42}$ (JCPDS PDF 26-0079) and orthorhombic α-$MoO_3$ (JCPDS PDF 76-1003) as labelled in Fig. 2. The formation of these intermediates aligns well with the aforementioned weight transitions in the TGA-DTA experiments. The subsequent decomposition of α-$MoO_3$ produced $Mo_8O_{23}$ and $Mo_4O_{11}$ intermediates, and generated a monoclinic $MoO_2$ phase at around 415 °C (see Scheme S2 in the ESI† for the reductive carburization steps). As the temperature is increased above 700 °C, it can be observed that the two major diffraction peaks at $2\theta = 5.33°$ and 7.51° of the $MoO_2$ phase begin to decrease. When the temperature is held at 800 °C, diffraction signals evolved at $2\theta = 5.99$, 7.01, 7.67, 7.98, and 8.85°. These peaks are assigned to orthorhombic $Mo_2C$ (JCPDS PDF 77-0720), which demonstrates that the sample transformed from $MoO_2$ to $Mo_2C$. These results provide evidence of a solid-state reaction between the molybdate and the carbon support.

### Morphology of the supported $Mo_2C$

The transmission electron microscopy (TEM) images shown in Fig. 3 display the morphology of $Mo_2C$/XC and $Mo_2C$/CNT (see Fig. S2 in the ESI† for magnified images and Fig. S3† for the lattice structure of $Mo_2C$/XC). The $Mo_2C$ particles on XC-72R and CNTs range from 7 to 15 nm (Fig. 3) and have an average

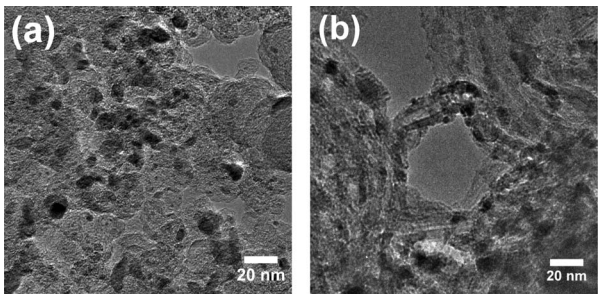


**Fig. 3** TEM images of the freshly prepared (a) $Mo_2C$/XC and (b) $Mo_2C$/CNT.

diameter of 12 nm, which agrees well with the grain size calculated from XRD results. The $Mo_2C$ particles are well-distributed on the carbon supports and no aggregation is observed.

### Electronic structures of anchored molybdenum carbides

We determined the charge states and electronic structures of nanostructured $Mo_2C$ catalysts by X-ray absorption near-edge structure (XANES) and extended X-ray absorption fine structure (EXAFS) spectroscopies. The Mo K edge XANES spectra from the carbon-supported Mo precursor (ammonium molybdate/C, green curve) in Fig. 4a show that the pre-edge at 20 004 eV and the edge shifts compared to Mo foil can be ascribed to the Mo(VI) oxidation state. In contrast, $Mo_2C$ (red curve and dotted grey curve) is easily differentiated by the shape of the white line above the Mo foil absorption edge. In Fig. 4b, the correlation of half step energy of the Mo K edge and the Mo valence state is shown. The Mo foil showed a zero-valence state. The bulk $Mo_2C$ presented a valence state at nearly zero, which agrees with the value reported elsewhere.[35] However, higher half-edge energies for $Mo_2C$/XC and $Mo_2C$/CNT than the bulk $Mo_2C$ are observed. This demonstrates a charge-transfer from molybdenum to carbon on the carbon-supported $Mo_2C$. Haslam *et al.* have recently demonstrated metal-to-ligand charge transfer on carbide materials.[36] Liu *et al.* have shown that the more positively charged the Mo atoms, the lower their d-band center.[20]

The details of the Mo binding environment can be described through the $k^2$-weighted EXAFS analysis in *r*-space shown in Fig. 4c. The differences between the $Mo_2C$ samples and their reference materials are apparent in the spectra, indicating that the atomic structures surrounding Mo in the $Mo_2C$ nanoparticles are significantly different from those in the Mo precursor, $MoO_2$, and Mo foil. The data were fitted with models constructed from the orthorhombic β-$Mo_2C$ structure. Good agreement was obtained between the fit and the experimental spectra (Fig. 5). Table 1 summarizes the obtained coordination numbers and bond lengths. We note that the lengths of the Mo–Mo bond obtained (2.98 and 3.29 Å) on $Mo_2C$/CNT and $Mo_2C$/XC are longer than that of pure Mo (2.73 Å), and are different from that of the bulk $Mo_2C$ (2.97 and 3.04 Å). The ratios of coordination number $N_{Mo-C}/N_{Mo-Mo}$ are 0.262 and 0.275 for $Mo_2C$/CNT and $Mo_2C$/XC, respectively, which are much higher than that obtained for the bulk $Mo_2C$.

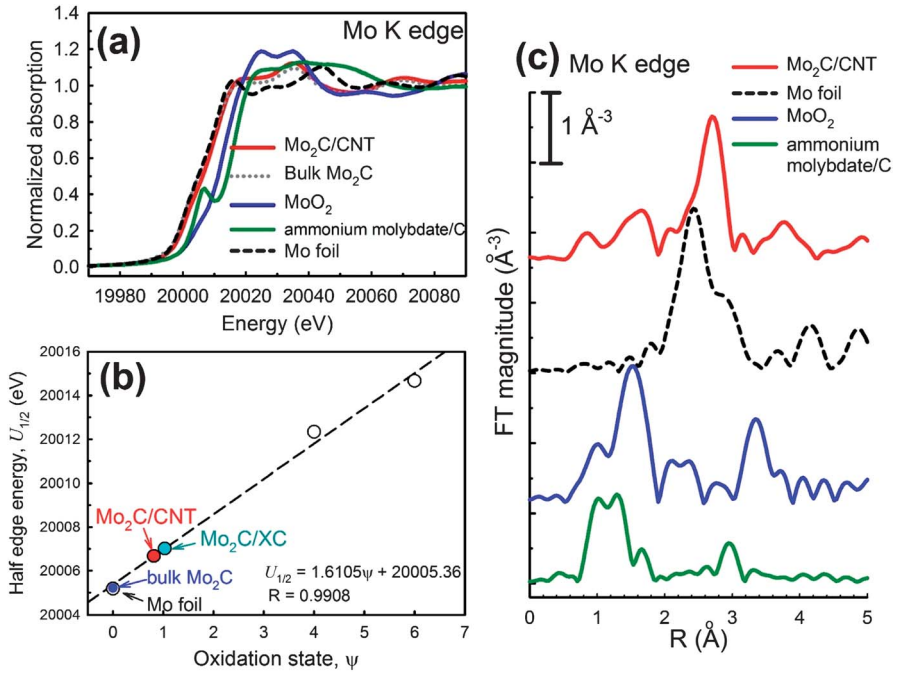


**Fig. 4** (a) XANES spectra at the Mo K edge from the CNT-supported $Mo_2C$, bulk $Mo_2C$, ammonium molybdate, molybdenum dioxide and Mo foil. (b) Correlation of the half step energy of the Mo K edge with the oxidation state of various molybdenum species. (c) $k^2$-weighted EXAFS Fourier transform magnitudes of the Mo K edge obtained from the CNT-supported $Mo_2C$, Mo foil, $MoO_2$ and ammonium molybdate.

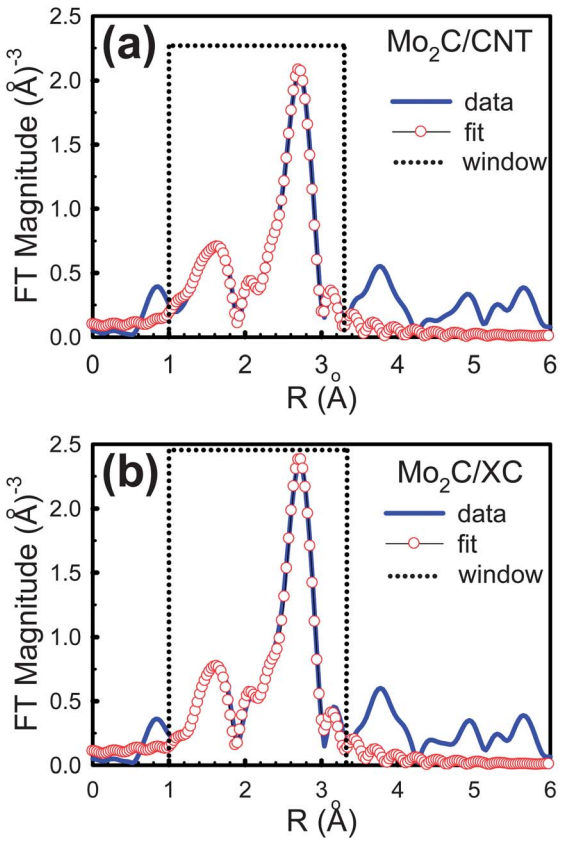


**Fig. 5** $k^2$-weighted EXAFS Fourier transform magnitudes and first-shell fit of the Mo K edge obtained from the CNT- and XC-72R-supported $Mo_2C$.

**Table 1** Bond lengths and coordination numbers determined by the EXAFS experiments

| Catalyst | $R_{Mo-C}$ | $N_{Mo-C}$ | $R_{Mo-Mo}$ | $N_{Mo-Mo}$ | $N_{Mo-C}/N_{Mo-Mo}$ |
|---|---|---|---|---|---|
| $Mo_2C$/CNT | 2.09 | 2.7 ± 0.16 | 2.98 | 8.3 ± 0.60 | 0.262 |
| | | | 3.29 | 2.0 ± 0.66 | |
| $Mo_2C$/XC | 2.09 | 2.8 ± 0.22 | 2.98 | 10.1 ± 0.48 | 0.275 |
| | | | 3.28 | 0.1 ± 0.35 | |
| Bulk $Mo_2C$ | 2.06 | 1.5 ± 0.46 | 2.97 | 4.9 ± 1.29 | 0.14 |
| | | | 3.04 | 6.5 ± 0.08 | |

This finding reveals that the $Mo_2C$ nanoparticles which are formed *in situ* are inlaid or anchored into the carbon supports. Recently, Lieber's research group has provided evidence that at sufficiently high temperature the metal carbide will grow toward the tube center on CNTs.[37,38] The covalent binding between $Mo_2C$ and the carbon support provides the following unique coupling effects on electrochemical properties. First, we would expect this kind of robust conjugation to help $Mo_2C$ catalysts coalesce strongly with the carbon supports, providing a resistance-less path suitable for fast electron transfer. Second, this conjugation hampers the aggregation of $Mo_2C$ nanoparticles, thereby facilitating highly reactive sites on the surfaces. Third, the anchored configuration induces a charge-transfer from molybdenum to carbon, which further downshifts the d-band center of molybdenum, and thereby decreases its hydrogen binding energy. This in turn favors the electrochemical desorption of $H_{ads}$ and leads to a relatively moderate Mo–H binding strength, resulting in the enhancement of the hydrogen evolution reaction. Molybdenum itself is known as a

strong hydrogen-binding metal owing to the high position of its d-band. Multilayer hydrogen uptake has been observed when a Mo surface is exposed to $H_2$ gas.

### Electrochemical performance

The electrocatalytic HER activities of $Mo_2C$/CNT and $Mo_2C$/XC were investigated on a carbon paper (Toray TGP-H-060) in $H_2$-saturated 0.1 M $HClO_4$ solution (see ESI† for experimental details). As a control experiment, a commercial Pt catalyst (E-TEK 20 wt% Pt on Vulcan XC-72R carbon black) and a Mo metal disk were also tested. The Pt/C catalyst exhibited high HER catalytic performance with an overpotential ($\eta_i$) of 14 mV ($\eta_i$ was defined as the potential at 1 mA $cm^{-2}$ of cathodic current density). The polarization curve ($i$–$V$ plot) recorded with a Mo metal electrode showed an overpotential of 223 mV for the HER (green line, Fig. 6). Compared to Mo metal, the electrode coated with the bulk $Mo_2C$ exhibited a slightly lower $\eta_i$ of 204 mV, which demonstrates that the presence of carbon in the Mo lattice favors proton reduction kinetics. In contrast, $Mo_2C$/CNT and $Mo_2C$/XC exhibited much smaller $\eta_i$ values of 63 and 105 mV, respectively (red and blue lines, Fig. 6), than Mo metal and the bulk $Mo_2C$, indicating that the robust structure formed by $Mo_2C$ and carbon supports reduces the energy input for activating the HER. For driving a current density of 10 mA $cm^{-2}$, $Mo_2C$/CNT only requires an overpotential of 152 mV, a performance which exceeds that of other nonprecious HER catalysts.[39–41] These results imply that faster electron transfer may occur on the CNT-supported $Mo_2C$ catalyst. To elucidate the charge-transfer mechanism, electrochemical impedance spectroscopy (EIS) analyses were performed on these catalysts.

### Electrochemical impedance spectroscopy analysis

The EIS measurements were carried out from 100 000 Hz to 0.002 Hz at selected values of the overpotential ($\eta$ = 0 to 250 mV). The Bode impedance curve of the bulk $Mo_2C$ recorded at $\eta$ = 100 mV (white circles, Fig. 7a) exhibited classical single time-constant behavior (see Fig. S5 for electrical equivalent circuit models in the ESI†). The data for XC-72R-supported (red circles, Fig. 7a) and CNT-supported (blue circles, Fig. 7a) $Mo_2C$ clearly reveal the presence of two time constants (Fig. S5b†). A two time-constant model has been used to describe the response of the HER on rough electrode surfaces.[42] The model consists of a series resistance, $R_s$, in series with two parallel branches; one is related to the charge-transfer process ($C_{d1}$ – $R_{ct}$); the other is related to the surface porosity. Here $R_s$ contains components arising from the resistance in the wiring ($R_{wiring}$), the resistance in the carbon paper ($R_{cp}$) and carbon black ($R_{cb}$), the resistance due to molybdenum carbide ($R_{carbide}$), and the solution resistance ($R_{soln}$). The value of $R_s$ is readily obtained from a Nyquist plot (Fig. S6 in the ESI†). Bare carbon paper, XC-72R on carbon paper and CNT on carbon paper showed series resistances of 1.40 ($R_{s0}$), 1.66 ($R_{s1}$) and 1.43 ($R_{s2}$) Ω $cm^2$, respectively. The bulk $Mo_2C$ on carbon paper presented a series resistance of 4.72 Ω $cm^2$ ($R'_{s0}$). $Mo_2C$/XC and $Mo_2C$/CNT electrodes showed small $R_s$ values of 2.70 Ω $cm^2$ ($R'_{s1}$) and 2.05 Ω $cm^2$ ($R'_{s2}$), respectively. Since $R_s$ comes from a sum of $R_{soln}$, $R_{wiring}$, $R_{cp}$ and $R_{carbide}$, the value of $R_{carbide}$ can be calculated by subtracting $R'_{si}$ from $R_{si}$. Accordingly, the $R_{carbide}$ values of the bulk $Mo_2C$, $Mo_2C$/XC and $Mo_2C$/CNT are 3.32, 1.04 and 0.62 Ω $cm^2$. This fact confirms that the anchoring of $Mo_2C$ on CNTs can preserve the high conductivity of CNTs; we consider that the higher electrochemical activity of $Mo_2C$/CNT compared with that of $Mo_2C$/XC is given by the greatly enhanced electron transport between the CNTs and $Mo_2C$ catalysts. A good approximation to the experimental data for $Mo_2C$/XC and $Mo_2C$/CNT was obtained using the two time-constant model (see Fig. S7 in the ESI†). The Nyquist plot for $Mo_2C$/CNT at overpotentials from 0 to 200 mV is presented in Fig. 7c. The charge-transfer resistance, $R_{ct}$, determined from the semicircle registered at low frequencies (high $Z'$), was found to be overpotential-dependent. The Nyquist profiles collected at $\eta$ = 100 mV on various $Mo_2C$ electrodes are compared in Fig. 7b. The $Mo_2C$/CNT electrode exhibited lower charge-transfer impedance (21 Ω $cm^2$) than did the $Mo_2C$/XC electrode (36.1 Ω $cm^2$), and much lower charge-transfer impedance than the bulk $Mo_2C$ (1600 Ω $cm^2$) as presented in Table 2.

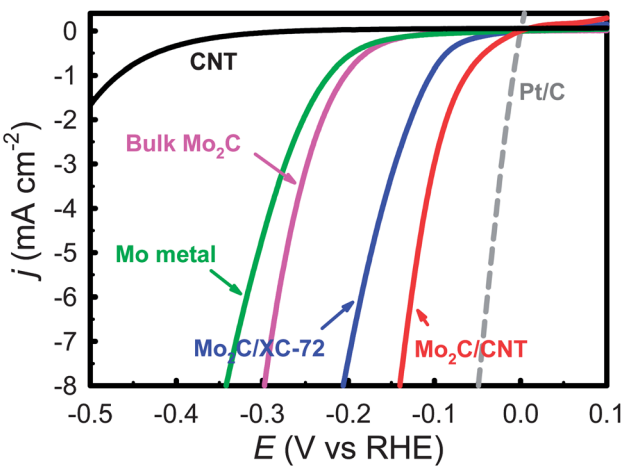


**Fig. 6** The polarization curves of nanostructured $Mo_2C$/CNT, $Mo_2C$/XC, bulk $Mo_2C$, Mo metal, Pt/C catalysts and pristine CNTs in a $H_2$-purged 0.1 M $HClO_4$ solution (scan rate 2 mV $s^{-1}$).

According to the two-electron-reaction models, cathodic hydrogen evolution in acidic aqueous media proceeds in two steps. First, the discharge step (Volmer reaction, for which the Tafel slope should be 116 mV $dec^{-1}$). Second, the electrochemical desorption step (Heyrovský reaction, for which the Tafel slope should be 40 mV $dec^{-1}$), or the Tafel recombination step (30 mV $dec^{-1}$). Early investigation into the dependence of the obtained impedance with applied potentials has demonstrated that the gradient of $\log(R_{ct}^{-1})$ *versus* potential corresponds to the Tafel slope of the proton discharging step. By fitting the impedance data of various $Mo_2C$ electrodes to the corresponding equivalent circuit models as aforementioned, one obtains the charge-transfer resistance $R_{ct}$ at different potentials. The overpotential is plotted *versus* the inverse $R_{ct}$ on a logarithmic scale, yielding a linear dependence as shown in Fig. 8. For the bulk $Mo_2C$, the slope ($b_R$) of 87.6 mV $dec^{-1}$ (Table 2) obtained from the linear curve suggests that hydrogen

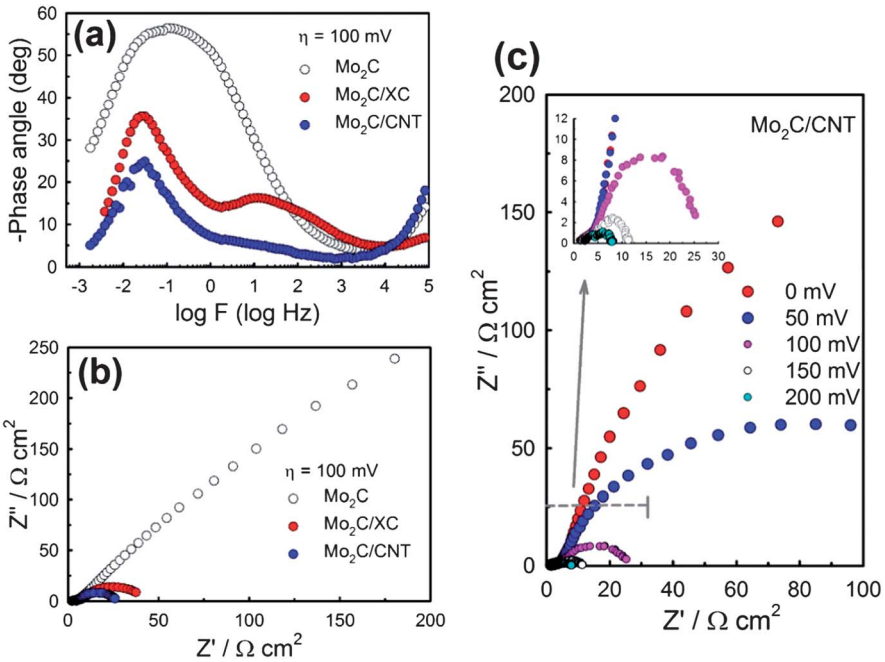


**Fig. 7** (a) Bode and (b) Nyquist plots of the bulk $Mo_2C$, $Mo_2C$/XC and $Mo_2C$/CNT recorded at $\eta = 100$ mV in 0.1 M $HClO_4$ solution. (c) Nyquist plots collected on $Mo_2C$/CNT at selected overpotentials (inset represents a close-up view of spectra at high frequencies).

evolution occurs *via* a Volmer–Heyrovský mechanism, in which the Volmer reaction is the rate-limiting step. For the XC-72R carbon- and CNT-supported $Mo_2C$, the smaller slopes of 59.4 and 55.2 mV $dec^{-1}$, respectively, suggest much faster proton discharge kinetics than that on the bulk $Mo_2C$. For these supported $Mo_2C$ electrodes, the values of $b_R$ have slopes similar to those obtained from a Tafel plot (see Table S1 in the ESI†).

At sufficiently small $\eta$ (mass transfer resistance $\ll$ charge transfer resistance), the exchange current density, $j_0$, can be determined *via* the equation:

$$R_{ct} = \frac{RT}{nFj_0}$$

where $R_{ct}$ is the charge transfer resistance at zero overpotential, $n$ represents the number of electrons exchanged, $F$ (96 485 C $mol^{-1}$) the Faraday constant, and $R$ (8.314 J $mol^{-1}$ $K^{-1}$) the gas constant. $Mo_2C$/CNT exhibited high $j_0$ ($1.4 \times 10^{-2}$ mA $cm^{-2}$, Table 2), which is higher than that of the bulk $Mo_2C$ by 1.3 orders of magnitude, and higher than the bulk Mo by 2.5 orders of magnitude. Considering the specific surface area of the $Mo_2C$ nanoparticles, the exchange current density of $Mo_2C$/CNT is slightly higher than that reported previously (Table S3 in the ESI†). Thus, the size effect of the CNT-supported $Mo_2C$ contributed significantly to its electrochemical performance.

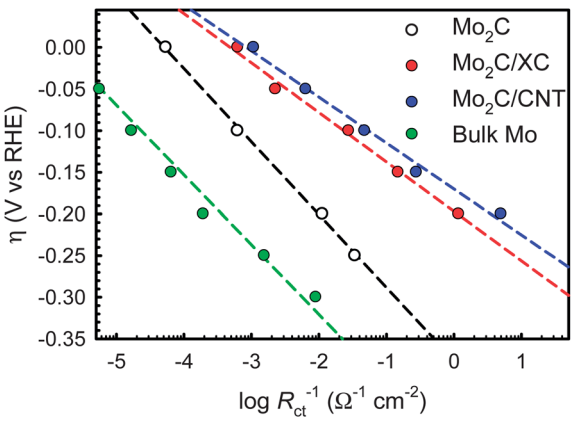


**Fig. 8** Semi-logarithmic plot of the inverse charge-transfer resistance, $R_{ct}^{-1}$, as a function of overpotential, $\eta$.

**Table 2** Overpotentials, charge-transfer resistances, Tafel slopes and exchange current densities collected in a $H_2$-saturated 0.1 M $HClO_4$ solution

| Catalyst | $\eta_i$ @ $j_{Cat}$ [a] = 1 mA $cm^{-2}$ (mV) | $\eta_f$ @ $j_{Cat}$ [b] = 1 mA $cm^{-2}$ (mV) | $R_{ct}$ @ $\eta = 100$ mV ($\Omega$ $cm^2$) | $b_R$ [c] (mV $dec^{-1}$) | $j_{0,R}$ [d] (mA $cm^{-2}$) |
|---|---|---|---|---|---|
| $Mo_2C$/CNT | 63 | 64 | 21.0 | 55.2 | $1.4 \times 10^{-2}$ |
| $Mo_2C$/XC | 105 | 283 | 36.1 | 59.4 | $8.1 \times 10^{-3}$ |
| $Mo_2C$ | 204 | 340 | 1600 | 87.6 | $6.9 \times 10^{-4}$ |
| Bulk Mo | 223 | 302 | $6.0 \times 10^4$ | 83.8 | $4.4 \times 10^{-5}$ |

[a] Initial overpotential at 1 mA $cm^{-2}$ of cathodic current ($j_{Cat}$). [b] Overpotential at 1 mA $cm^{-2}$ after potential sweeps for 3000 cycles between −0.3 and +0.63 V *vs.* RHE. [c] Slopes obtained from the plot of $\log(R_{ct}^{-1})$ *versus* overpotential in Fig. 7. [d] Exchange current density calculated by the charge-transfer resistance at zero overpotential.

 

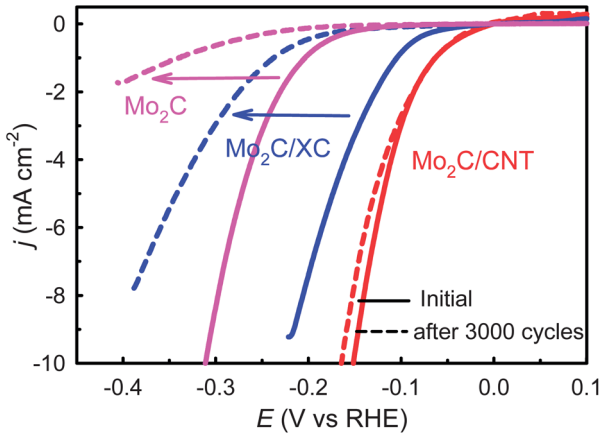


**Fig. 9** The polarization curves before and after potential sweeps (−0.3 to +0.63 V *vs.* RHE) for 3000 cycles in 0.1 M $HClO_4$ solution.

### Durability in acidic media

A promising catalyst material for the HER should exhibit not only high activity but also good durability. To evaluate the long-term performance of the $Mo_2C$ catalysts in acidic aqueous media, potential sweeps were conducted. After 3000 cycles of potential sweeps between −300 and +630 mV *vs.* RHE, the $\eta_f$ at $j_{Cat} = 1$ mA $cm^{-2}$ of the polarization curve shown in Fig. 9 remains almost unchanged for the $Mo_2C$/CNT catalyst. A long-term electrolysis experiment also demonstrated that $Mo_2C$/CNT is durable for the HER up to 24 h (see Fig. S9 in the ESI†). In contrast, the analogous $Mo_2C$/XC and the bulk $Mo_2C$ catalysts (as well as the Mo electrode) show apparent degradation of the activity (see $\eta_f$ in Table 2). These results demonstrate that the coupling effect between $Mo_2C$ and CNT plays an important role for significant improvement of the durability in an acidic environment.

## Conclusions

We have employed earth abundant and inexpensive components to develop a heterogeneous electrocatalytic hydrogen evolving system. The as-prepared $Mo_2C$/CNT displayed superior electrocatalytic performance for the hydrogen evolution reaction with small overpotential (63 mV for driving 1 mA $cm^{-2}$ of current density) compared to the XC-72R carbon-supported $Mo_2C$, bulk $Mo_2C$ and Mo metal electrodes. Near-edge XAS analysis has demonstrated that an increase in the $N_{Mo-C}/N_{Mo-Mo}$ ratio induces the transfer of negative charge from molybdenum to carbon. The EIS results clearly demonstrate that incorporation of $Mo_2C$ onto a carbon support brings about a significant enhancement in the exchange current density, a remarkable reduction in charge-transfer resistance, and a change in the HER mechanism. The interplay between electronic and support effects is found to be responsible for this superior performance. First, a solid-state carburization process keeps the $Mo_2C$ particles clean from char coverage and affords the growth of anchored $Mo_2C$ nanoparticles free of aggregation on CNTs. The robust $Mo_2C$–CNT (covalent binding) structure provides highly exposed reactive sites. Second, the carbide ligand effect modifies the d-electron configuration of the $Mo_2C$ particles and imparts a moderate Mo–H binding energy. Third, $Mo_2C$/CNT exhibits faster kinetics for electron transfer than does the basal plane of XC-72R carbon, since electronic coupling to the underlying CNT substrate in a covalent conjugation affords rapid electron transport to the $Mo_2C$ particles. In acidic media, the $Mo_2C$/CNT catalysts can be used with very little attenuation. Therefore, the present results suggest that this novel $Mo_2C$/CNT nanocomposite holds promise as a Pt-free high-performance HER catalyst.

## Materials and methods

### Synthesis of supported molybdenum carbides

Carbon nanotube- and Vulcan XC-72R carbon black-supported molybdenum carbides ($Mo_2C$/CNT and $Mo_2C$/XC, respectively) were prepared by carburization of carbon-supported ammonium molybdate ($(NH_4)_6Mo_7O_{24}\cdot 4H_2O$, Aldrich). A typical procedure for preparing the carbides is as follows: 197 mg of ammonium molybdate and 250 mg of Vulcan XC-72R carbon black were mixed in water to obtain a loading of 30 wt% total Mo metal. The slurry was dried at 130 °C. For carburization, the solid mixture was annealed in a tube furnace with a 100 ml $min^{-1}$ Ar flow from ambient to 800 °C at a rate of 13 °C $min^{-1}$ and then held at 800 °C for 2 h. Ar was kept purging through the reactor when the reactor was cooled to ambient temperature. Carbon nanotube (multi-wall carbon nanotubes, purity >95%, length of 1–2 μm, average diameter of 20 nm, American Elements)-supported molybdenum carbide was prepared by the same procedure as above. The pristine carbon nanotubes were pretreated with a 3 N HCl aqueous solution and then were washed with a copious of Milli-Q water to remove excess $Cl^-$.

### Thermogravimetric/differential thermal analysis (TG/DTA)

Thermogravimetric measurements and differential thermal analysis were performed with a Perkin Elmer Diamond thermogravimetric/differential thermal analyzer. The sample was placed in an alumina sample holder. Measurements in pure argon with a flow rate of 100 ml $min^{-1}$ were carried out over a temperature range of 50–800 °C at a heating rate of 20 °C $min^{-1}$ and then held at 800 °C for 2 h.

### Electron microscopy

High-resolution transmission electron microscopy (TEM) imaging was performed using a JEOL JEM3000F TEM equipped with a field emission gun and a Gatan imaging filter (GIF). The instrument was operated at 300 kV.

### Powder X-ray diffraction spectroscopy

Measurements were taken with a Rigaku Miniflex II diffractometer using Cu Kα radiation ($\lambda = 1.54056$ Å). The patterns were collected from 5 to 85° at a scanning rate of 2° $min^{-1}$, with a step size of 0.01°. The grain size of the $Mo_2C$ particles was calculated using the Debye–Scherrer equation,

$$D_{hkl} = \frac{k_{hkl}\lambda}{\beta_{hkl}\cos(\theta)}$$

where $\lambda$ is the wavelength of the X-rays ($\lambda = 1.54$ Å) and $\beta_{hkl}$ (or FWHM) is the angular line width.

### *In situ* time-resolved synchrotron XRD

The measurements were performed at the X7B beamline at NSLS to detail the intermediates and $Mo_2C$ structures during carburization. The instrument parameters (Thompson Cox Hastings profile coefficients) were derived from the fit of a $LaB_6$ reference pattern. Approximately 5 mg of the carbon-supported ammonium molybdate were loaded in a 1 mm quartz reactor that was attached to a flow system. The sample was annealed at a heating rate of 2.5 °C $min^{-1}$ from 25 °C to 400 °C, then at 5 °C $min^{-1}$ up to 800 °C, and kept at 800 °C for 2 hours (800 °C is for accelerating the carburization process). A small resistance heater was wrapped around the reactor capillary, and the temperature was monitored with a thin chromel alumel thermocouple placed inside the capillary near the sample. We maintained a 3.5 mL $m^{-1}$ in He gas flow throughout the annealing process. The wavelength of X-ray used was 0.3184 Å. XRD patterns were recorded on a Mar345 image plate detector during annealing; the recording time for a spectrum is 80 seconds. Details of the synchrotron XRD experiment were described earlier.[43,44]

### Synchrotron X-ray absorption spectroscopy

The X-ray absorption spectroscopy (XAS) measurements were undertaken at the National Synchrotron Light Source (NSLS), BNL at the X18B beamlines. The measurements were carried out at the Mo K edge (20 000 eV) at room temperature. The XAS data were acquired in both the transmission and fluorescence modes, although the data presented in this report were obtained in the former. The data acquired were processed and analyzed by Athena and Artemis software.[45]

### Electrochemical measurements

The electrodes for the electrochemical measurements were fabricated as follows. Catalyst ink was prepared by mixing carbon-supported $Mo_2C$ catalyst powder with 50% isopropanol aqueous solution (1 mL for 100 mg of electrocatalyst). 20% Nafion dispersion (DuPont) was added (50 mg solid Nafion for 100 mg of catalyst) to the catalyst slurry. Catalyst coating on the gas diffusion layer (Toray TGP-H-060 30 wt% wet-proofing carbon paper) with 1 $cm^2$ active area was fabricated by brushing the catalyst ink on. The catalyst loading was 2 mg catalyst per $cm^2$. The electrode was then dried under vacuum at 60 °C. The electrolytes for electrochemical measurements were prepared from Optima perchloric acid obtained from Fisher and Milli-Q UV-plus water (Millipore). Commercial Pt/C (10 wt%) from E-TEK and bulk $Mo_2C$ powder (Alfa Aesar, 99.5%) were used as received. An Ag/AgCl/KCl (3 M) electrode was used with a double-junction chamber as a reference, and all potentials, *E*, are quoted with respect to a reversible hydrogen electrode (RHE). All electrochemical experiments are carried out at ambient temperature (25 °C) in a 0.1 M $HClO_4$ solution. A control experiment was carried out in a pH = 7 phosphate buffer solution (see Fig. S10†). The driving current was low, possibly due to the low transport kinetics of hydroxide ions.

## Acknowledgements

This work was carried out at Brookhaven National Laboratory (BNL) under contract DE-AC02-98CH10886 with the U.S. Department of Energy (DOE) and supported by BNL Laboratory Directed Research and Development (LDRD) Project no. 10-015. Beamlines X18B at the NSLS are supported in part by the Synchrotron Catalysis Consortium, U.S. Department of Energy Grant no. DE-FG02-05ER15688. XRD and TGA/DTA are carried out at the Center for Functional Nanomaterials, Brookhaven National Laboratory.

## Notes and references

1 T. F. Jaramillo, K. P. Jørgensen, J. Bonde, J. H. Nielsen, S. Horch and I. Chorkendorff, *Science*, 2007, **317**, 100–102.
2 H. I. Karunadasa, E. Montalvo, Y. Sun, M. Majda, J. R. Long and C. J. Chang, *Science*, 2012, **335**, 698–702.
3 D. Merki, H. Vrubel, L. Rovelli, S. Fierro and X. L. Hu, *Chem. Sci.*, 2012, **3**, 2515–2525.
4 D. Merki and X. L. Hu, *Energy Environ. Sci.*, 2011, **4**, 3878–3888.
5 M. Wang, L. Chen and L. C. Sun, *Energy Environ. Sci.*, 2012, **5**, 6763–6778.
6 I. Nikolov, T. Vitanov and V. Nikolova, *J. Power Sources*, 1980, **5**, 197–206.
7 H. Zheng, J. Huang, W. Wang and C. Ma, *Electrochem. Commun.*, 2005, **7**, 1045–1049.
8 J. S. Jang, D. J. Ham, N. Lakshminarasimhan, W. y. Choi and J. S. Lee, *Appl. Catal., A*, 2008, **346**, 149–154.
9 F. Harnisch, G. Sievers and U. Schröder, *Appl. Catal., B*, 2009, **89**, 455–458.
10 D. V. Esposito, S. T. Hunt, Y. C. Kimmel and J. G. Chen, *J. Am. Chem. Soc.*, 2012, **134**, 3025–3033.
11 S. Wirth, F. Harnisch, M. Weinmann and U. Schroder, *Appl. Catal., B*, 2012, **126**, 225–230.
12 P. D. Tran, M. Nguyen, S. S. Pramana, A. Bhattacharjee, S. Y. Chiam, J. Fize, M. J. Field, V. Artero, L. H. Wong, J. Loo and J. Barber, *Energy Environ. Sci.*, 2012, **5**, 8912–8916.
13 D. Merki, S. Fierro, H. Vrubel and X. L. Hu, *Chem. Sci.*, 2011, **2**, 1262–1267.
14 A. B. Laursen, S. Kegnaes, S. Dahl and I. Chorkendorff, *Energy Environ. Sci.*, 2012, **5**, 5577–5591.
15 R. B. Levy and M. Boudart, *Science*, 1973, **181**, 547–549.
16 Z. W. Chen, D. Higgins, A. P. Yu, L. Zhang and J. J. Zhang, *Energy Environ. Sci.*, 2011, **4**, 3167–3192.
17 D. V. Esposito, S. T. Hunt, A. L. Stottlemyer, K. D. Dobson, B. E. McCandless, R. W. Birkmire and J. G. Chen, *Angew. Chem., Int. Ed.*, 2010, **49**, 9859–9862.

 

18 D. V. Esposito and J. G. Chen, *Energy Environ. Sci.*, 2011, **4**, 3900–3912.
19 M. C. Weidman, D. V. Esposito, Y.-C. Hsu and J. G. Chen, *J. Power Sources*, 2012, **202**, 11–17.
20 P. Liu, J. A. Rodriguez and J. T. Muckerman, *J. Phys. Chem. B*, 2004, **108**, 15662–15670.
21 A. Celzard, J. F. Mareche, G. Furdin, V. Fierro, C. Sayag and J. Pielaszek, *Green Chem.*, 2005, **7**, 784–792.
22 N. M. Schweitzer, J. A. Schaidle, O. K. Ezekoye, X. Pan, S. Linic and L. T. Thompson, *J. Am. Chem. Soc.*, 2011, **133**, 2378–2381.
23 J. Han, J. Duan, P. Chen, H. Lou, X. Zheng and H. Hong, *ChemSusChem*, 2012, **5**, 727–733.
24 M. Pang, C. Y. Liu, W. Xia, M. Muhler and C. H. Liang, *Green Chem.*, 2012, **14**, 1272–1276.
25 H. Vrubel and X. Hu, *Angew. Chem., Int. Ed.*, 2012, **51**, 12703–12706.
26 A. Hanif, T. C. Xiao, A. P. E. York, J. Sloan and M. L. H. Green, *Chem. Mater.*, 2002, **14**, 1009–1015.
27 C. A. Wolden, A. Pickerell, T. Gawai, S. Parks, J. Hensley and J. D. Way, *ACS Appl. Mater. Interfaces*, 2011, **3**, 517–521.
28 H. M. Wang, X. H. Wang, M. H. Zhang, X. Y. Du, W. Li and K. Y. Tao, *Chem. Mater.*, 2007, **19**, 1801–1807.
29 S. Chouzier, T. Czeri, M. Roy-Auberger, C. Pichon, C. Geantet, M. Vrinat and P. Afanasiev, *J. Solid State Chem.*, 2011, **184**, 2668–2677.
30 M. K. Kolel-Veetil, S. B. Qadri, M. Osofsky and T. M. Keller, *Chem. Mater.*, 2005, **17**, 6101–6107.
31 E. V. Matus, I. Z. Ismagilov, O. B. Sukhova, V. I. Zaikovskii, L. T. Tsikoza, Z. R. Ismagilov and J. A. Moulijn, *Ind. Eng. Chem. Res.*, 2007, **46**, 4063–4074.
32 W.-F. Chen, K. Sasaki, C. Ma, A. I. Frenkel, N. Marinkovic, J. T. Muckerman, Y. Zhu and R. R. Adzic, *Angew. Chem., Int. Ed.*, 2012, **51**, 6131–6135.
33 Z. L. Yin, X. H. Li, G. Z. Zhou, Q. S. Zhao and S. Y. Chen, *Trans. Nonferrous Met. Soc. China*, 1996, **6**, 26–28.
34 I. Salagean, D. Trestian and E. Segal, *Rev. Roum. Chim.*, 1973, **18**, 1537–1546.
35 J. G. Chen, *Chem. Rev.*, 1996, **96**, 1477–1498.
36 G. E. Haslam, K. Sato, T. Mizokawa, X. Y. Chin and G. T. Burstein, *Appl. Phys. Lett.*, 2012, 100.
37 H. J. Dai, E. W. Wong, Y. Z. Lu, S. S. Fan and C. M. Lieber, *Nature*, 1995, **375**, 769–772.
38 E. W. Wong, B. W. Maynor, L. D. Burns and C. M. Lieber, *Chem. Mater.*, 1996, **8**, 2041–2046.
39 Z. Chen, D. Cummins, B. N. Reinecke, E. Clark, M. K. Sunkara and T. F. Jaramillo, *Nano Lett.*, 2011, **11**, 4168–4175.
40 H. Vrubel, D. Merki and X. Hu, *Energy Environ. Sci.*, 2012, **5**, 6136–6144.
41 Y. Y. Li, H. Wang, L. Xie, Y. Liang, G. Hong and H. Dai, *J. Am. Chem. Soc.*, 2011, **133**, 7296–7299.
42 B. Łosiewicz, A. Budniok, E. Rówiński, E. Łągiewka and A. Lasia, *Int. J. Hydrogen Energy*, 2004, **29**, 145–157.
43 J. A. Rodriguez, J. C. Hanson, W. Wen, X. Wang, J. L. Brito, A. Martínez-Arias and M. Fernández-García, *Catal. Today*, 2009, **145**, 188–194.
44 L. Barrio, A. Kubacka, G. Zhou, M. Estrella, A. Martinez-Arias, J. C. Hanson, M. Fernández-Garcia and J. A. Rodriguez, *J. Phys. Chem. C*, 2010, **114**, 12689–12697.
45 B. Ravel and M. Newville, *J. Synchrotron Radiat.*, 2005, **12**, 537–541.